Simulation of longitudinal stent deformation in a patient-specific coronary artery

Georgios E. Ragkousis[a], Nick Curzen[b,c] , Neil W. Bressloff[a*]

[a]*Computational Engineering & Design Group, Faculty of Engineering & the Environment, University of Southampton, Southampton, UK*

[b]*University Hospitals Southampton NHS Foundation Trust*

[c] *Faculty of Medicine, University of Southampton, Southampton, UK*

Article type: original article

Keywords: Longitudinal stent deformation, stents, stent malapposition, finite element analysis, patient specific model

[*] *Corresponding author: Computational Engineering & Design Group, Building 176- Room 5031, University of Southampton, Boldrewood campus, Burgess Road, Southampton, Hampshire, SO16 7QF, UK*
Email: N.W.Bressloff@soton.ac.uk
Tel. +44(0)2380 595473
Fax. +44(0)2380 594813

Abstract

In percutaneous coronary intervention (PCI), stent malapposition is a common complication often leading to stent thrombosis (ST). More recently, it has also been associated with longitudinal stent deformation (LSD) normally occurring through contact of a post balloon catheter tip and the protruding malapposed stent struts.

The aim of this study was to assess the longitudinal integrity of first and second generation drug eluting stents in a patient specific coronary artery segment and to compare the range of variation of applied loads with those reported elsewhere. We successfully validated computational models of three drug-eluting stent designs when assessed for longitudinal deformation. We then reconstructed a patient specific stenosed right coronary artery segment by fusing angiographic and intravascular ultrasound (IVUS) images from a real case. Within this model the mechanical behaviour of the same stents along with a modified device was compared. Specifically, after the deployment of each device, a compressive point load of 0.3N was applied on the most malapposed strut proximally to the models. Results indicate that predicted stent longitudinal strength (i) is significantly different between the stent platforms in a manner consistent with physical testing in a laboratory environment, (ii) shows a smaller range of variation for simulations of *in vivo* performance relative to models of *in vitro* experiments, and (iii) the modified stent design demonstrated considerably higher longitudinal integrity. Interestingly, stent longitudinal stability may differ drastically after a localised *in vivo* force compared to a distributed *in vitro* force.

1. Introduction

Percutaneous coronary intervention (PCI) is now the dominant method of revascularization, with proven symptomatic and prognostic efficacy. Since the introduction of drug-eluting stents (DES) there has been a marked reduction in events associated with stent failure, in particular in-stent restenosis (ISR). However, DES have been associated with allergic reactions, stent malapposition and inflammation leading to early and late stent thrombosis (ST) [1]. Furthermore, there are on-going concerns about the attritional nature of the potential sources of failure of PCI, including ISR, ST and, more recently, longitudinal stent deformation (LSD).

Stent malapposition has been proven clinically to be connected with late stent thrombosis [2, 3] and can be categorised into acute malapposition and late malapposition. Clinical studies [2, 4, 5] have shown that each type of malapposition is connected with several factors, such as reference diameter, balloon pressure, longer lesions, longer stents, more than one stent or stent overlap. In those studies stent malapposition was investigated by intravascular means such as intravascular ultrasound (IVUS) or optical coherence tomography (OCT). When malapposition is observed clinically, post stent deployment with non-compliant balloon dilation is used to further reshape the stent. Such post-deployment techniques, including also re-wiring or IVUS, can potentially contribute to stent distortion. Studies [6-8] indicate that those deformations are more likely to occur when the proximal struts are incompletely apposed.

There has been a well-established association between stent design and adverse events. Factors including particularly strut thickness [9], but also geometry, have been correlated with ISR, ST and LSD. It is apparent that the iterative process of design in DES has led to reduced ISR (along with anti-inflammatory stent coatings) with reduction in strut thickness, but that an increased reporting of LSD may be a consequence of this evolution [6-8, 10]. It is therefore important that new stent designs are tested as thoroughly as possible to detect potential flaws.

To date, there have been two experimental (engineering) studies shedding light on LSD [11, 12], and one computational study [13] investigating the longitudinal integrity of small stent segments (two rings) after free expansion, but no patient specific computational studies have been reported. It is likely that sophisticated computer modelling will have an increasing role in this process of validation and testing.

In this study, a patient specific artery segment was constructed from angiographic images; a computer model was developed for the deployment in this segment of different coronary stent architectures based upon one first generation and two second generation DES; post-deployment malapposition was assessed; and the effect of stent malapposition and stent architecture on the response of the devices to a compressive longitudinal force was modelled. The proposed approach allows quantification and visualisation of LSD along the entire length of the model, in contrast to the currently used LSD measurement techniques based on IVUS cross sectional images. We sought to validate this model as a potential tool for assessment of stent design behaviour and to test it using previously reported physical bench testing data.

2. Materials and Methods

A patient-specific right coronary artery (RCA) reconstruction was carried out by fusing multiple IVUS frames and two bi-plane angiographic images from an actual case. The geometry segment was reconstructed in IVUS-Angio Tool, a freely available software [14], and Rhinoceros 5.0 (Robert McNeel & Associates, USA), a commercially available NURBS package. Stent designs were created in Rhinoceros 5.0. For the simulations, the commercially available FEA solver, ABAQUS/ Explicit v.6-12 (Simulia Corporation, USA) was used.

2.1. Geometry, meshes and constitutive models

The vessel reconstruction procedure has been presented in detail in our previous work [15], (and is summarized in Appendix A.1).

Many constitutive models have been used to characterize arteries with the most representative being that reported by Holzapfel et al. [16]. In the current study, the wall of the vessel is modeled by using a hyperelastic, neo-Hookean strain energy function. The assumption was based on the fact that the average material of the vessel wall is plaque and the difficulty to extract the plaque composition from the IVUS images; therefore, constitutive parameters for a soft plaque were selected. The latter is proposed by Wong et al. [17] and its parameters were used within our group previously [18]. Thus, the strain energy per unit of reference volume is

$$U = C_{10}(\bar{I}_1 - 3) + \frac{1}{D_1}(J - 1)^2 \quad (1)$$

where C_{10} and D_1 are temperature-dependent material parameters related to the shear and bulk moduli ($\mu_0 = 2C_{10}$, $K_0 = 2/D_1$), $\bar{I}_1$ is the first deviatoric strain invariant defined as

$$\bar{I}_1 = \bar{\lambda}_1^{2} + \bar{\lambda}_2^{2} + \bar{\lambda}_3^{2} \quad (2)$$

where the deviatoric stretches $\bar{\lambda}_i = J^{-1/3}\lambda_i$, J is the total volume ratio, J is the elastic volume ratio, and λ_i are the principal stretches.

The vessel was meshed using eight node linear brick reduced integration elements with hourglass control (ABAQUS element type C3D8R). The wall thickness was discretised by two elements. The total number of elements which were used to mesh the reconstructed vessel was 21214, and

32019 nodes, based on a mesh sensitivity study (i.e. accepting differences of maximum and minimum displacements between coarse and finer meshes less than 2%). The elements were checked for invalid geometry so as to avoid numerical inaccuracies.

For the stents, firstly we generated two balloon expandable stent models whose architecture is closely based upon contemporary stent designs used in the clinical arena. Stent A, which resembles the Promus Element (Boston Scientific, USA), is an 'offset peak to peak stent' and stent B, which resembles Xience (Abbott Lab., USA), is an 'in-phase, peak to valley stent design' as categorised in Prabhu et al. [12]. Secondly, we modified Stent A by constructing two additional connectors between the first two proximal hoops (see Appendix A.2) and we model an old out-of-phase, peak-to-peak device, which resembles the Cypher (Johnson & Johnson co., USA), used by this group previously [19]. Figure 1A&B depict the computer-aided design (CAD) generation of stent B. Both current generation stents were constructed based on the unit strut creation by NURBS curves. The unit strut is offset to the stent width and then extruded to the strut thickness. The solid unit strut is copied along the circumference so as to form a full circumferential ring which is then copied along the longitudinal axis to generate the flat 3D solid stent architecture. The final step contains the transformation of the flat stent onto a cylinder so as to represent a cylindrical stent configuration, as shown in Figure 1B. Thereafter, our design approach (see Appendix A.3) is to geometrically transform the stent on to the reconstructed catheter line so as to avoid the additional numerical analysis step of stent implantation and positioning (c.f. Figure 1C). Table 1 provides information about the stent designs, alloys and number of links which were assumed for the investigated devices.

The stent platforms are defined as isotropic elastic-plastic materials. Their material properties have been adopted by O'Brien et al. [20](c.f. Table 2). The stents were meshed using eight node linear brick, reduced integration elements with hourglass control (ABAQUS element type C3D8R). Stents A, B, and C were discretised by assigning two elements along the strut thickness and three elements along the strut width resulting in 34786, 46216, 35286 elements, respectively. Stent D was discretised by assigning four elements along the strut thickness and three elements along the strut width resulting in 76352 elements. The discretization of the stents was based on mesh sensitivity studies (i.e. accepting differences of maximum and minimum displacements between coarse and finer meshes less than 2%).

2.2. *FEA simulations*

All the events of the FEA analysis were simulated as quasi-static where the inertia forces arise only from the deformation of structure and are not dominating in the analysis. Throughout the whole period of each step, the kinetic and internal energies of the deforming materials were monitored so as to keep their ratio less than 5%, as indicated for a quasi-static event [21]. Since it is computationally impractical to model the process in its natural time period, the analysis was based on the extraction of the fundamental frequency (first natural frequency) of the stent models by running frequency analysis in ABAQUS/Standard 6.12. It is recommended that the load to be applied over a period calculated from the fundamental frequency has to be ten to fifty times longer than the lowest frequency. The chosen loading rate was chosen based on a period sensitivity test (the kinetic energy and the maximum displacement of the model had differences less than 1% between different simulated time periods).

2.2.1. Simulated bench test validation

In order to validate the ability of our model to detect and/or reproduce longitudinal compression, we simulated previously published [11] physical bench testing in which a compressive force was applied as a distributed longitudinal load. In order to mimic the experimental method, the devices were constrained distally during the compression test and only 10mm of their length was exposed to the compressive load. The load was imposed proximally to the devices and distributed on the edges of the circumferential crowns. The LSD was calculated from the displacements of the nodes on which the distributed load was imposed.

2.2.2. Virtual stent expansion in the reconstructed vessel

In order to reduce computational cost, two different design simulation approaches were followed and compared in previous work [15], (summarised in Appendix A.3). The first approach consists of three steps (crimping, positioning, and expansion) and the second of two steps (crimping and expansion). Thereafter, a comparison between two expansion techniques was carried out in order to simplify the deployment step (c.f. Appendix A.4). In the first method, for stent deployment, a realistic five folded balloon was used whilst, in the second method, a deformable surface was used. The comparisons have indicated that similar results can be taken from the investigated methodologies and, as a result, the less computationally expensive methodologies are followed in this study. The contact between the stent and the vessel was modelled by defining hard normal behaviour and a 0.05 friction coefficient for the tangential contact property [22, 23]. All other contacts (including self-contacts) were modelled with 0.2 friction coefficient for the tangential contact behaviour [24, 25].

Stents were implanted in the reconstructed vessel at the same location, aligned at the proximal ends. Then, the devices were crimped and expanded by deformable surfaces with controlled predefined displacement, and shown in Figure 2. This method has been proven an optimal choice when simulating stent expansions, as it is less computationally expensive, and it provides similar results (with a balloon expansion) regarding the final stent shape (and thus, the stresses and strains the stent is subjected to) when reaching its nominal diameter [25]. At the end of the expansion step, the relative stent malapposition was evaluated by measuring the minimum distance between the upper nodes of the stent and the inner nodes of the vessel.

2.2.3. Virtual longitudinal deformation of the stents

To undertake the virtual assessment of longitudinal integrity of the stents, following deployment, a compressive load was imposed on the stent strut that was most malapposed, labelled as CL in Figure 2. This strut was chosen because it represents the area most likely to come into contact with the leading edge of a post stent device moving forwards on the coronary line. The direction of the compressive load is represented by the white arrow in Figure 2. The LSD was calculated from the displacement of the node to which the localised load was imposed.

3. **Results**

3.1. Validation of the stent longitudinal behaviour

Figure 3 depicts images of the investigated stents expanded to a diameter of 3.00mm and deformed by a compressive load applied proximally to each device. The stent compression (millimetres) against the compressive force (Newton) for the investigated devices is depicted in Figure 4. Stent A was compressed with 0.4N and Stent B was compressed with 1.2N resulting in displacements of 4.75mm and 5.14mm, respectively. This numerical bench test shows that the modelled stents, A & B, demonstrated similar longitudinal deformation to that presented by Ormiston et al. [11], and their experimental results for corresponding devices are superimposed on the same figure (c.f. Figure 4). Therefore, one can observe that the numerical bench test is well matched with the experimental results within the acceptable range of 2.8% to 5% of the final displacement. Stents C and D were compressed with 1N and 3N resulting in displacements of 4.80mm and 1.16mm, respectively.

3.2. Stent Malapposition

The contour plots of the 3D stent malapposition along with cross sectional images proximal, middle and distal to the devices (broken lines) are depicted in Figure 5. All the devices show similar results in this regard: specifically, stent malapposition occurs predominantly at the proximal edge. The maximum distance between a stent node and a vessel wall node is 0.3775mm, 0.3483mm, 0.3329mm, and 0.3325 for Stents A, B, C, and D, respectively.

3.3. LSD within the reconstructed coronary segment

The LSD was evaluated virtually after stent deployment in the reconstructed segment by applying a localised compressive load of 0.3N proximally to the stent on the malapposed struts of all models as shown in Figure 2. Relative performance between the stents can be assessed by considering the force needed to displace by 0.5mm the node at which the load is applied. This displacement also coincides with the onset of noticeable protrusion of struts in the lumen as depicted in the insets of Figure 6 (cross-sectional images are depicted proximally to the model-broken lines-where significant strut protrusion for Stents A and B occurs due to the LSD). In Figure 7 the longitudinal deformation is depicted with respect to the compressive load. Forces of 0.19N and 0.29N, respectively, are needed for stents A and B. In contrast, Stent C does not deform significantly in terms of strut protrusion (Figure 6) in the lumen although the node at which the load is applied almost reaches a displacement of 0.5mm at the peak load of 0.3N (Figure 7). Stent D shows negligible compression both in terms of strut protrusion or displacement (c.f. Figures 6 and 7).

4. Discussion

In a recent study [26], a new methodology was developed to study stent malapposition numerically with finite element analysis. In our study a similar technique was used to calculate stent malapposition numerically. Our technique was based on the shortest distance between the nodes which lie on the outer surface of the stent and the nodes which lie on the inner surface of the reconstructed vessel (relative malapposition). The results showed that for this patient specific case, stent malapposition is similar for all the investigated devices. This suggests that the proximal malapposition is primarily dependent on the variation in vessel diameter and the associated diameter mismatch that occurs when sizing the stent on the distal diameter.

Longitudinal deformation results in protrusion of stent struts in the lumen (Figure 6) hence potentially obstructing further manipulation [10]. Most cases reported of LSD involve very thin device platforms with open cell designs (offset peak to peak). Whilst reducing strut thickness and increasing the area between the struts improve the stent flexibility, stent deliverability and stent conformability, the subsequent compromise of stent longitudinal integrity may produce reduced resistance to potential compression loads. Two recent experimental studies [11, 12] which have investigated current generation stents have reported similar results and have emphasized the importance of the number and the angulation of the connectors between the hoops to resist compression. Specifically, the offset peak to peak device with the open cell design had the poorest behaviour in longitudinal integrity. In contrast, devices with more than two connectors were relatively resistant to compressive loads.

In this computational modelling study, from the compression simulations, we observed that stent A with two connectors (with 45^0 connector angulation) showed significantly less longitudinal strength than stent B with three connectors (aligned with the longitudinal axis of the device). This is consistent with the concept that stents with two connectors are more susceptible to LSD than devices with three connectors. At the other end of the spectrum, we observed considerable resistance to LSD in a stent with six connectors (Stent D) in which a force of 3N compresses the stent only 1mm. From the LSD-graph (Figure 4) Stent A seems to have a more linear behaviour than stent B which demonstrates an initial “hardening” to the first 2mm. This behaviour is consistent with the experimental laboratory-derived results taken from Ormiston et al. [11] and the virtual LSD simulations extracted from the present study, shown in Figure 7.

For the bench test, stent C demonstrated a significant stiffer response than stent A to compressive loads but inferior to stent B. Modifying stent A by constructing additional connectors proximally, the longitudinal integrity increases significantly (more than the double amount of force was required for a 5mm compression, Figure 4). Also, it is observed that the proximal end of the modified stent is not distorted by the compression, Figure 3, a fact that can explain the “hardening” of the stent’s response between 4mm and 4.5mm in Figure 4.

Interestingly, the computer simulations of deformation in the RCA segment, Figure 7, indicate that devices A, B and C do not oppose the load proportionally to the bench tests (c.f. Figure 4). Only Stent D shows similar stiff behaviour in both cases. The virtual compressive simulations indicate that Stent C opposes the compressive force successfully and no significant distortion of the device was observed (c.f. Figures 6 and 7). Also, in contrast to the bench test, Stent C demonstrates higher resistance than Stent B (c.f. Figures 4 and 7). This indicates that in contrast to bench tests, *in vivo* failure of different stent devices may not occur at such drastically different localised loads.

From our model using compression simulations, it is clear that LSD is dependent on the number of the stent connectors and their angulation with the stent longitudinal axis. Apart from the number of the connectors, considerations should be made on the phase angle between stents' sequential hoops. Out-of-phase devices seem to resist more under compressive loads. Further research is needed to investigate variations in the proximal phase angle of the circumferential rings in the offset peak-to-peak device.

This study, to the best of the authors' knowledge, is the first to investigate longitudinal deformation and stent malapposition virtually in a patient specific reconstructed vessel. Such numerical studies for research purposes can provide useful information in 3D along the entire length of the models. Figures 5 and 6 illustrate very clearly the investigated clinical problems and it is strongly believed that such quantitative information can predict and further improve the associated complications by optimising the implanted device in any given challenging geometry.

4.1. Limitations and future directions

This study has some limitations. Firstly, for the purposes of this work, only one patient specific case was used and therefore the results cannot necessarily be generalised to other lesions. Second, in our model, the vessel wall is assumed to be hyperelastic and isotropic comprising a single layer. This is due to the fact that our reconstruction method is based on IVUS images from which the plaque composition is difficult to extract. Current imaging techniques such as computed tomography (CT), magnetic resonance imaging (MRI) and IVUS in combination with contrast agents can provide a better differentiation between the arterial layers and the plaque. Therefore, a multi-layer model will of course have some influence on the results.

As shown by Gee et al. [27], taking the in-vivo geometry (reconstructed by the imaging data) of abdominal aortic aneurysms as stress-free is not suitable for computational simulations as this results in non-physical deformations under realistic loading. In a recent study [28], the vessel wall pre-stretch was incorporated in a computational framework to investigate the positional stability of aortic endografts. It was shown that one of the factors affecting the positional stability is the variation of friction coefficient. However, due to the comparative rationale of this study, tissue pre-stretch and arterial blood pressure (averaged 100 mmHg) was neglected. Also, the friction coefficient was chosen to be uniform between the contact surfaces. Future studies will incorporate more analytical vessel models taking into account the different arterial layers and the pre-stress/pre-strain state of the vessel wall. Moreover, the pulsatile compressive loads imposed by the myocardium on the coronary arteries have to be further investigated.

Deformable surfaces were used to expand the stents instead of a balloon model. However, for this patient specific model, we compared the stent malapposition after the surface expansion with a realistic five folded balloon expansion and we obtained similar results in terms of stent malapposition (see the Appendix A.4). This method has also shown to provide similar computational results (final stent shape) with a balloon expansion strategy as shown in previous studies [13, 25]. At the end, the investigated stent devices were generated in commercial CAD software. As a result, they are not identical to the real devices they resemble.

5. Conclusions

In conclusion, we have constructed a computational engineering model of a coronary lesion that has allowed for simulation of stent malapposition and LSD in three stent designs and a modified device that are based upon one first generation and two second generation DES. Our results are consistent with previous laboratory based experiments of LSD. Also, the simulations suggest that the threshold where the stent loses its longitudinal resistance may differ *in vivo* compared to *in vitro*, particularly with respect to the range of variation in loads needed to deform second generation drug eluting coronary stents We believe that such a model may provide a useful tool for testing the integrity and validation of new stent designs.

Conflict of interest statement

Prof. Curzen has received unrestricted research funding from Medtronic and Haemonetics. He has received speaking and/or consultancy fees from Boston Scientific, St. Jude Medical, Medtronic, Abbott Vascular, Lilly/DS and Haemonetics. Prof. Bressloff and Mr. Ragkousis have no conflict of interest to declare.

Appendix A

A.1. *RCA 3D reconstruction*

Several IVUS frames and two orthogonal bi-planar angiographic images have to be collected and imported into the IVUS Angio-Tool where the catheter path definition and the lumen with the vessel wall segmentation are carried out. The catheter path is defined by both LAO (left anterior oblique) and RAO (right anterior oblique) angiographic images which differ by approximately 90°; the LAO is shown in Figure 8A. The segmentation of lumen and media-adventitia border contours is carried out by active contours models [29] (c.f. Figure 8B). This editing can then be written as a point-cloud in a text file which is imported in Rhinoceros 5.0 for further processing. In Rhinoceros 5.0, the realistic 3D IVUS pullback path is reconstructed as the intersection of the two bi-plane orthogonal curve extrusions. The resultant curve is scaled down to its real dimensions according to:

$$L_{ivus} = \frac{N_{frames}}{f} * S_{pullback} \tag{3}$$

where normally $f = 30\, frames/sec$ and $S_{pullback} = 0.5\, mm/sec$. The resultant 3D catheter curve comprises the backbone on which the lumen and the wall contours are positioned after being converted into real dimensions calculated from IVUS-Angio Tool. At each location point on the curve, the Frenet trihedron is calculated (Figure 8C). The precise position of the IVUS contours on the catheter line is formulated by orientating the contours at each location point with geometrical transformations which map three units vectors {X,Y,Z} (defined on each cross section contour) to the Frenet trihedron {T,N,B} (at each location point). The final orientation is then calculated by rotating all the contours by a specific angle around the T vector such as when re-projecting the reconstructed vessel onto the RAO and LAO views, a satisfactory matching is accomplished. Figure 8D shows the 3D realistic representations of the reconstructed lumen from LAO and RAO.

A.2. *Modified Stent*

In order to improve the longitudinal integrity of Stent A, we constructed two additional connectors in each of the first two proximal hoops. The planar sketch of the modified design is depicted in Figure 9. The circles illustrate the four additional connectors proximally on the device.

A.3. *Comparison of two Simulation Design Methodologies*

In order to reduce the computational time, we compared two different simulation design methodologies. The first consists of three steps (crimping, positioning, and expansion), whilst the second consists of two steps (crimping, expansion). Figure 10 illustrates the different approach followed. Specifically, in the first approach (from the top left and anticlockwise), the positioning of the stent into the diseased site is undertaken within the FEA package, a fact that increases the total computational time. On the other hand, the second approach (from the top left and clockwise) positions the stent system into the vessel within the CAD software with geometrical transformation which maps the central axis of the stent system on the reconstructed IVUS catheter line. In Figure 11, boxplots of the average nodal Von Mises stresses of the stent, for the two simulation methodologies, are illustrated indicating almost identical results at the end of the stent expansion in terms of stent malapposition. The discrepancy of maximum, minimum and average Von Mises stress yield values within the acceptable range of 0.7-3.7% (see Table 3).

A.4. *Simplification of the expansion method*

We performed stent deployment with a deformable surface and a realistic five folded balloon (see Figure 12). Thereafter, we plotted cumulative distribution function (CDF) graphs of the resulting malapposition at the end of the expansion steps (see Figure 13). The CDF graphs indicate that for both expansion methods in this patient specific case, the stent malapposition is identical following device deployment.

Acknowledgements

Competing interests: Prof. Curzen has received unrestricted research funding from Medtronic and Haemonetics. He has received speaking and/or consultancy fees from Boston Scientific, St. Jude Medical, Medtronic, Abbott Vascular, Lilly/DS and Haemonetics. Prof. Bressloff and Mr. Ragkousis have no conflict of interest to declare.

Funding: None

Ethical approval: Not required

References

[1] Cook S, Ladich E, Nakazawa G, Eshtehardi P, Neidhart M, Vogel R, et al. Correlation of Intravascular Ultrasound Findings With Histopathological Analysis of Thrombus Aspirates in Patients With Very Late Drug-Eluting Stent Thrombosis. Circulation. 2009;120:391-9.

[2] Cook S, Wenaweser P, Togni M, Billinger M, Morger C, Seiler C, et al. Incomplete Stent Apposition and Very Late Stent Thrombosis After Drug-Eluting Stent Implantation. Circulation. 2007;115:2426-34.

[3] Ozaki Y, Okumura M, Ismail TF, Naruse H, Hattori K, Kan S, et al. The fate of incomplete stent apposition with drug-eluting stents: an optical coherence tomography-based natural history study. European Heart Journal. 2010;31:1470–6.

[4] Hong M-K, Mintz GS, Lee CW, Park D-W, Park K-M, Lee B-K, et al. Late Stent Malapposition After Drug-Eluting Stent Implantation: An Intravascular Ultrasound Analysis With Long-Term Follow-Up. Circulation. 2006;113:414-9.

[5] van der Hoeven BL, Liem S-S, Dijkstra J, Bergheanu SC, Putter H, Antoni ML, et al. Stent Malapposition After Sirolimus-Eluting and Bare-Metal Stent Implantation in Patients with ST-Segment Elevation Myocardial Infarction: Acute and 9-Month Intravascular Ultrasound Results of the MISSION! Intervention Study. JACC: Cardiovascular Interventions. 2008;1:192-201.

[6] Hanratty C, Walsh S. Longitudinal compression: a “new” complication with modern coronary stent platforms – time to think beyond deliverability? EuroIntervention. 2011;7:872-7.

[7] Robinson AD, Schreiber TL, Sobh MA, Grines CL. Deformation, Longitudinal Shortening, and Accordion of an Ion Stent. Journal of Interventional Cardiology. 2011;24:493-5.

[8] Williams PD, Mamas MA, Morgan KP, El-Omar M, Clarke B, Bainbridge A, et al. Longitudinal stent deformation: a retrospective analysis of frequency and mechanisms. EuroIntervention. 2012;8:267-74.

[9] Kastrati A, Mehilli J, Dirschinger J, Pache J, Ulm K, Schühlen H, et al. Restenosis after coronary placement of various stent types. The American Journal of Cardiology. 2001;87:34-9.

[10] Mortier P, De Beule M. Stent design back in the picture: an engineering perspective on longitudinal stent compression. EuroIntervention. 2011;7:773-5.

[11] Ormiston JA, Webber B, Webster MWI. Stent Longitudinal Integrity: Bench Insights Into a Clinical Problem. JACC: Cardiovascular Interventions. 2011;4:1310-7.

[12] Prabhu S, Schikorr T, Mahmoud T, Jacobs J, Potgieter A, Simonton CA. Engineering assessment of the longitudinal compression behaviour of contemporary coronary stents. EuroIntervention. 2012;8:275-81.

[13] Grogan JA, Leen SB, McHugh PE. Comparing coronary stent material performance on a common geometric platform through simulated bench testing. Journal of the Mechanical Behavior of Biomedical Materials. 2012;12:129-38.

[14] CERTH/ITI. 3D Ivus angio-tool. 2.1 ed2011.

[15] Ragkousis G, Curzen N, Bressloff N. Patient specific stent malapposition in challenging anatomy: An fea methodology to understand numerically the extend of malapposition of latest generation stents. Proceedings of ASME Summer Bioengineering Conference. Oregon: American Society of Mechanical Engineering; 2013.

[16] Holzapfel GA, Sommer G, Gasser CT, Regitnig P. Determination of layer-specific mechanical properties of human coronary arteries with nonatherosclerotic intimal thickening and

related constitutive modeling. American Journal of Physiology - Heart and Circulatory Physiology. 2005;289:H2048-H58.

[17] Wong HC, Cho KN, Tang WC. Bending of a Stented Atherosclerotic Artery. Proceedings of the COMSOL Conference. Boston2009.

[18] Pant S, Bressloff N, Limbert G. Geometry parameterization and multidisciplinary constrained optimization of coronary stents. Biomechanics and Modeling in Mechanobiology. 2012;11:61-82.

[19] Pant S, Limbert G, Curzen NP, Bressloff NW. Multiobjective design optimisation of coronary stents. Biomaterials. 2011;32:7755-73.

[20] O'Brien BJ, Stinson JS, Larsen SR, Eppihimer MJ, Carroll WM. A platinum–chromium steel for cardiovascular stents. Biomaterials. 2010;31:3755-61.

[21] SIMULIA. ABAQUS 6.12. 2013.

[22] Dunn A, Zaveri T, Keselowsky B, Sawyer WG. Macroscopic Friction Coefficient Measurements on Living Endothelial Cells. Tribology Letters. 2007;27:233-8.

[23] Auricchio F, Conti M, De Beule M, De Santis G, Verhegghe B. Carotid artery stenting simulation: From patient-specific images to finite element analysis. Medical Engineering & Physics. 2011;33:281-9.

[24] Mortier P, Holzapfel G, Beule M, Loo D, Taeymans Y, Segers P, et al. A Novel Simulation Strategy for Stent Insertion and Deployment in Curved Coronary Bifurcations: Comparison of Three Drug-Eluting Stents. Annals of Biomedical Engineering. 2010;38:88-99.

[25] De Beule M, Mortier P, Carlier SG, Verhegghe B, Van Impe R, Verdonck P. Realistic finite element-based stent design: The impact of balloon folding. Journal of Biomechanics. 2008;41:383-9.

[26] Mortier P, De Beule M, Segers P, Verdonck P, Verhegghe B. Virtual bench testing of new generation coronary stents. EuroIntervention. 2011;7:369-76.

[27] Gee MW, Reeps C, Eckstein HH, Wall WA. Prestressing in finite deformation abdominal aortic aneurysm simulation. Journal of Biomechanics. 2009;42:1732-9.

[28] Prasad A, Xiao N, Gong X-Y, Zarins C, Figueroa CA. A computational framework for investigating the positional stability of aortic endografts. Biomechanics and Modeling in Mechanobiology. 2013;12:869-87.

[29] Giannoglou GD, Chatzizisis YS, Koutkias V, Kompatsiaris I, Papadogiorgaki M, Mezaris V, et al. A novel active contour model for fully automated segmentation of intravascular ultrasound images: In vivo validation in human coronary arteries. Computers in Biology and Medicine. 2007;37:1292-302.

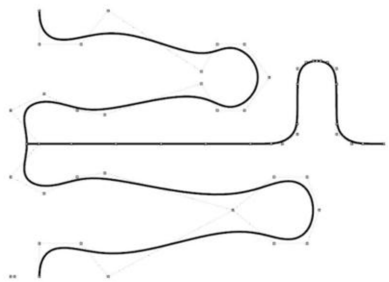

a

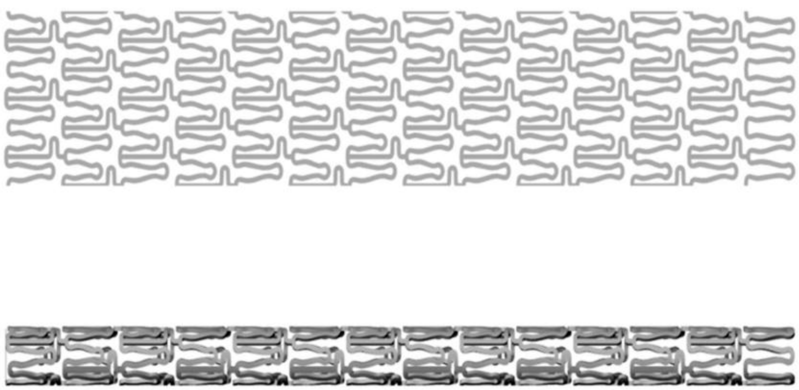

b

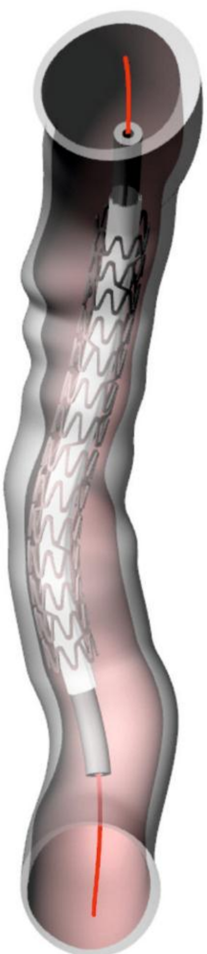

c

Figure 1: CAD model generation

A) Five degree NURBS curves are depicted for the unit strut generation. B) The solid stent B is generated based on the five degree curve. C) Stent A translated onto the 3D reconstructed IVUS pullback catheter path (red line).

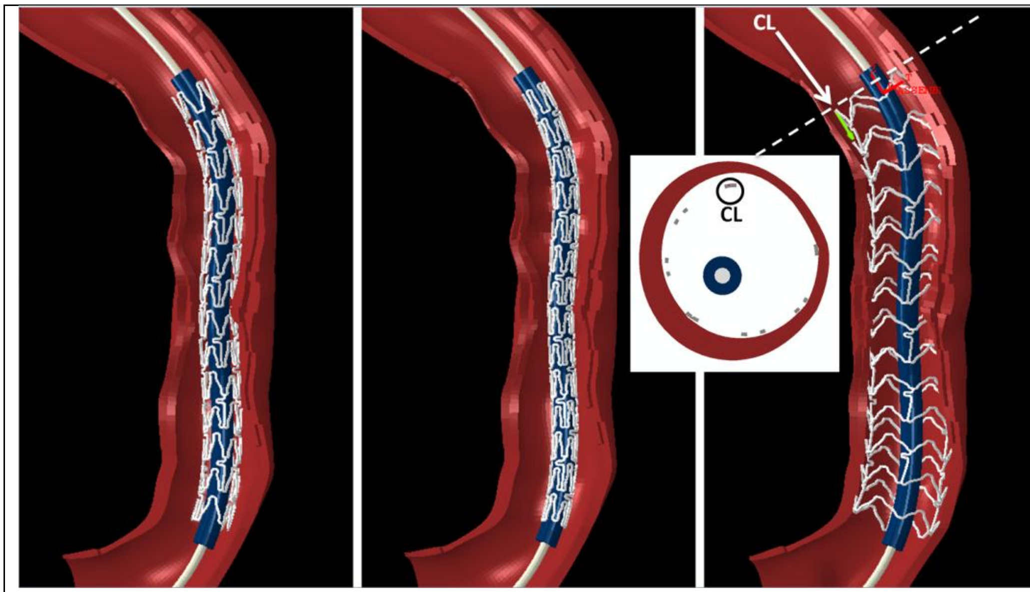

Figure 2: Simulation Steps

Stent pre-flown on the catheter shaft (left), stent crimped on the catheter shaft (centre) and stent expanded from the 3D reconstructed catheter line (right). The imposed compressive load, CL (white arrow), proximally to the model with respect to a reference coordinate system and the cross-sectional image at the proximal edge of the stent are depicted (right).

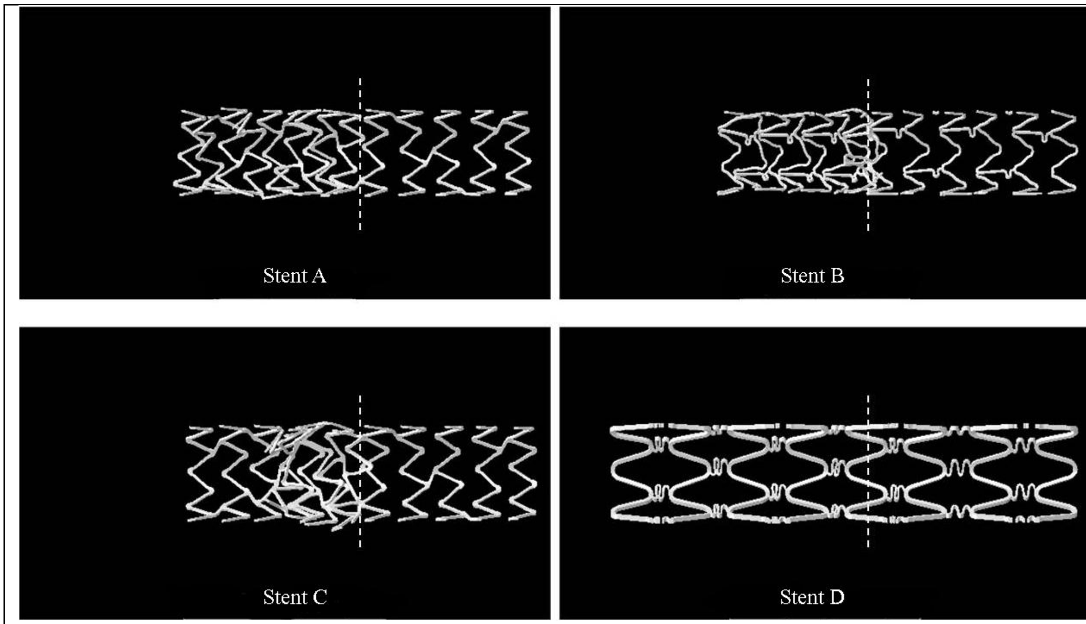

Figure 3: Simulated bench test

Virtual bench test validating the longitudinal integrity of the investigated stents. The devices were expanded to a nominal diameter of 3mm and were constrained along their length so that 10mm of the stents were exposed to the distributed load (broken lines).

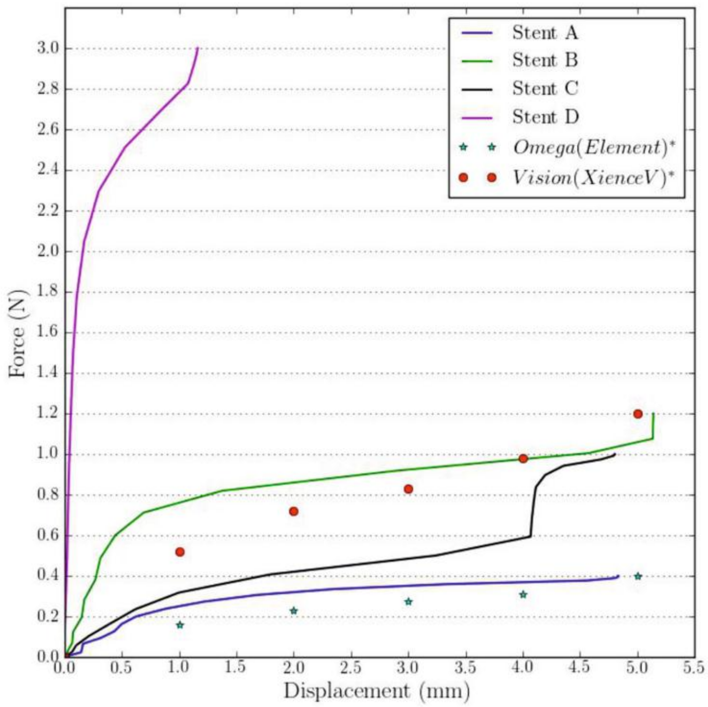

Figure 4: Distributed compressive load and stent deformation

Compressive force and stent longitudinal deformation after numerical bench test. Superimposed experimental results (*) published by Ormiston et al [11] showing LSD in good agreement with our numerical results.

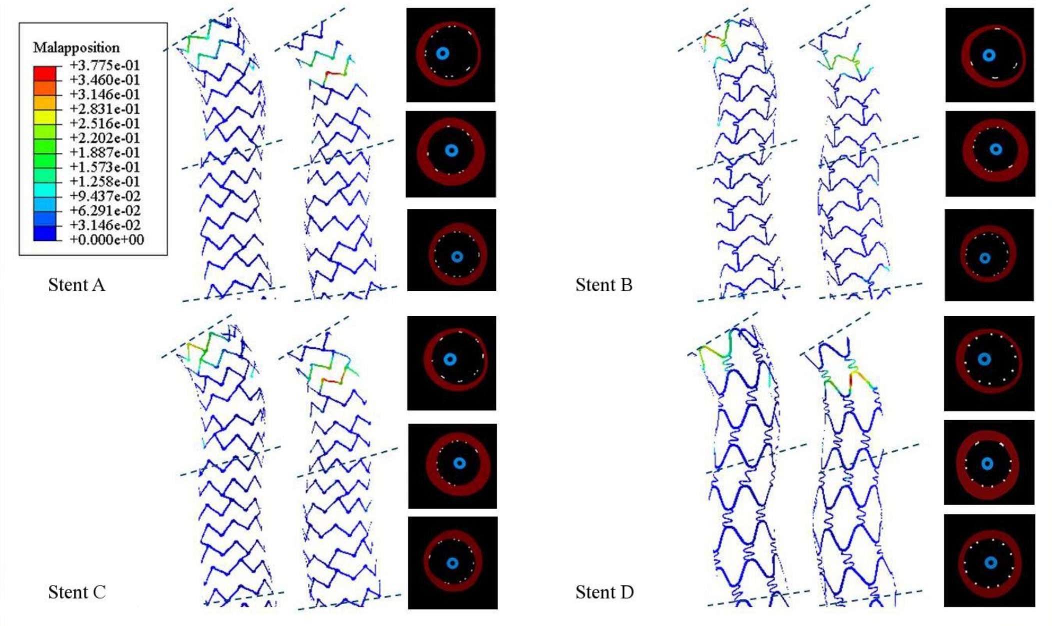

Figure 5: Virtual Stent Malapposition

Stent malapposition (mm) after the expansion of the investigated devices. For each device, cross sectional images were taken at the proximal, middle and distal area (broken lines) of the model.

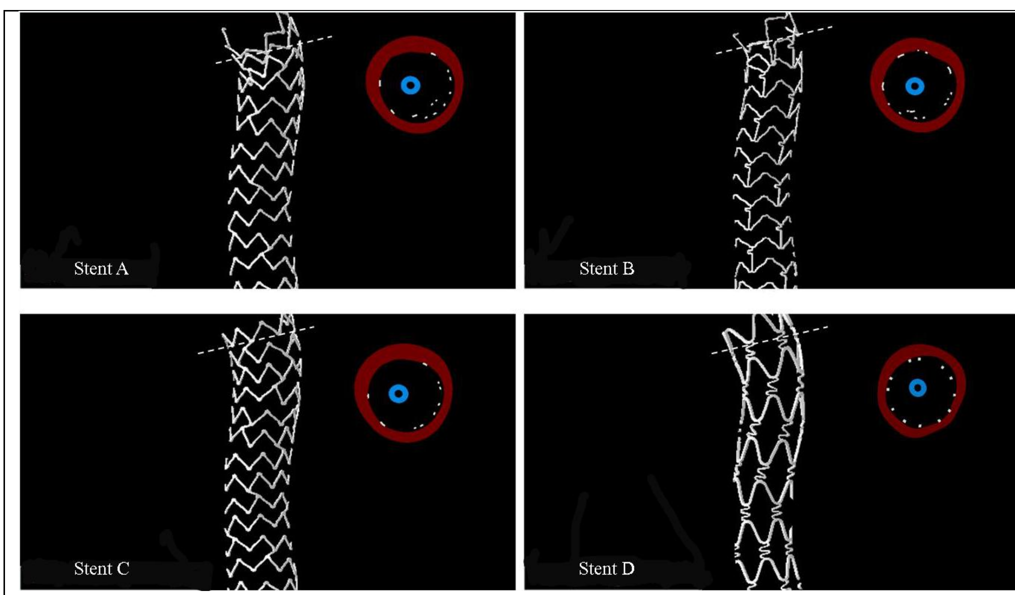

Figure 6: Vitual stent longitudinal deformation

Stent computer models cut longitudinally after they had been compressed by a 0.3N localised load at the most malapposed strut proximally to the device. For each model, a cross sectional image was taken proximally (broken lines) so as to identify potential strut protrusion due to stent deformation.

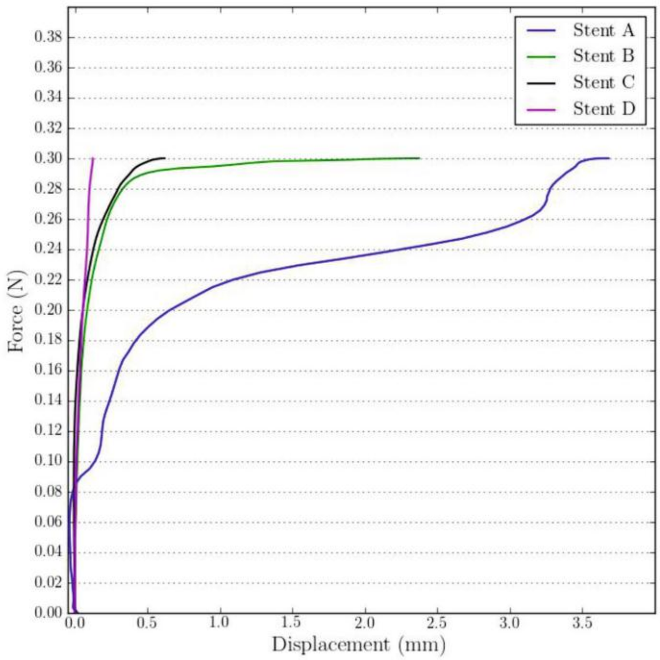

Figure 7: Localised compressive load and stent deformation

Stent compression (mm) against a compressive point load. For all devices, a 0.3N load was applied smoothly so as to evaluate longitudinal resistance.

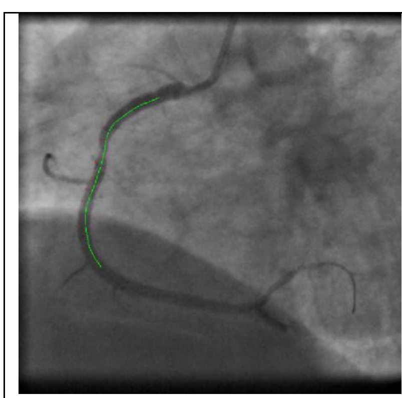

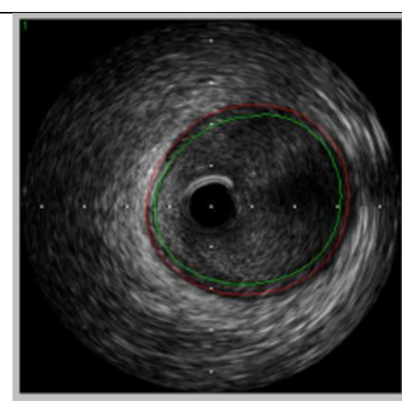

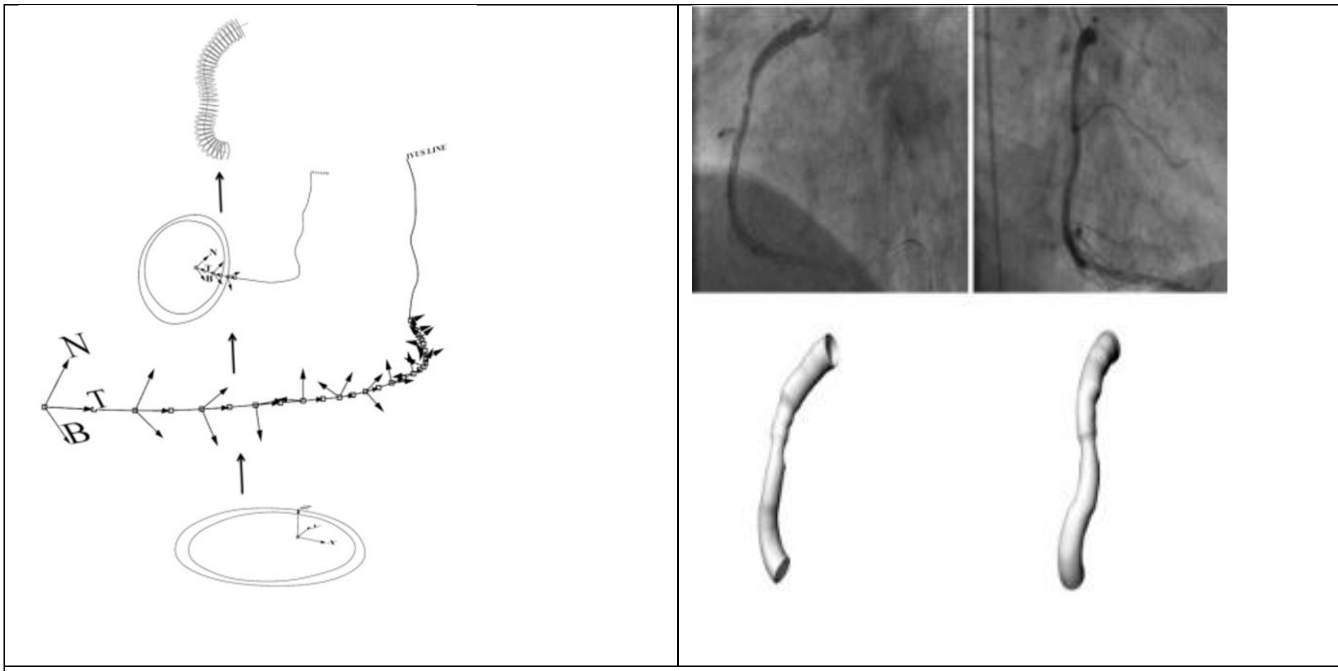

Figure 8. Right coronary artery (RCA) reconstruction. (A) Left anterior oblique (LAO) angiographic image. (B) Intravascular ultrasound (IVUS) image segmentation in IVUS Angio-Tool. (C) Segmented cross section orientation on the reconstructed catheter line according to the calculated Frenet trihedron at each position point. (D) Final reconstructed lumen surface from LAO and RAO.

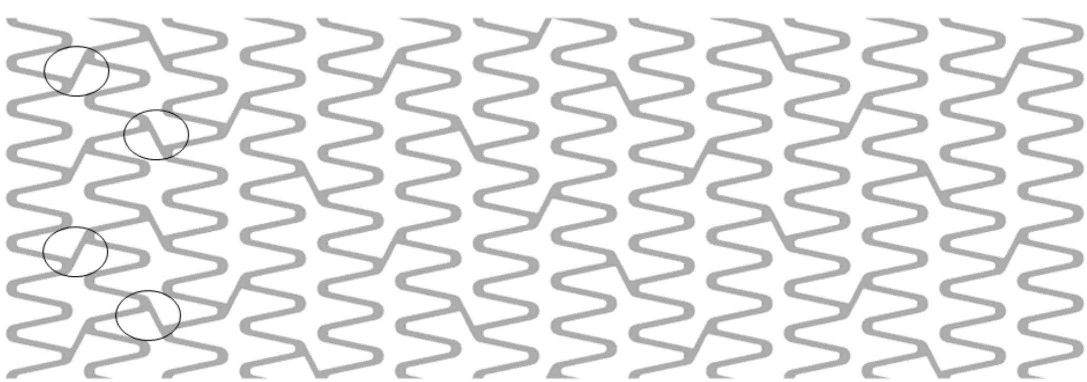

Figure 9. Planar sketch of the modified stent C. In total, four additional connectors were constructed at the proximal end of the device.

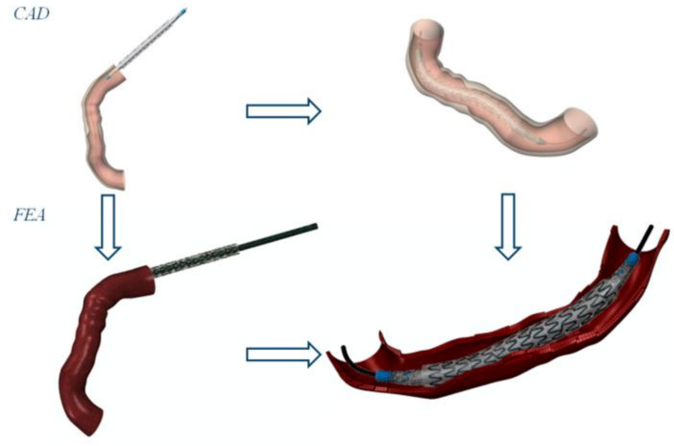

Figure 10. Illustration of the two simulation design strategies. Approach 1, from the top left and anticlockwise to the bottom right. Approach 2, from the top left and clockwise to the bottom right.

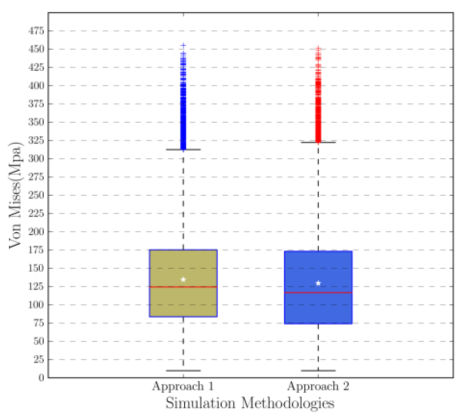

Figure 11. Boxplots of the average Von Mises distribution of the expanded stent between the two simulation approaches.

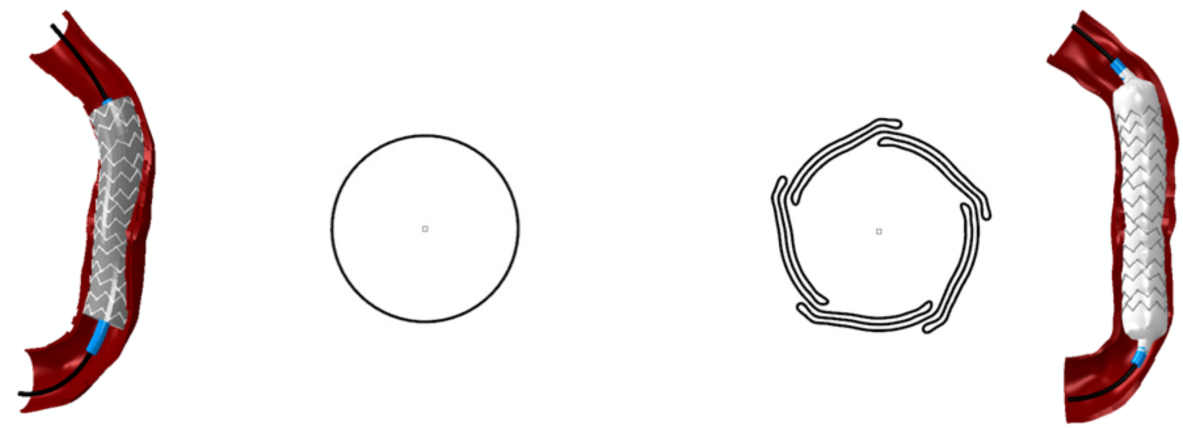

Figure 12. Illustration of stent expansion with a deformable surface (left) and a realistic five folded balloon (right). Cross sections of the expansion means are depicted next to each model.

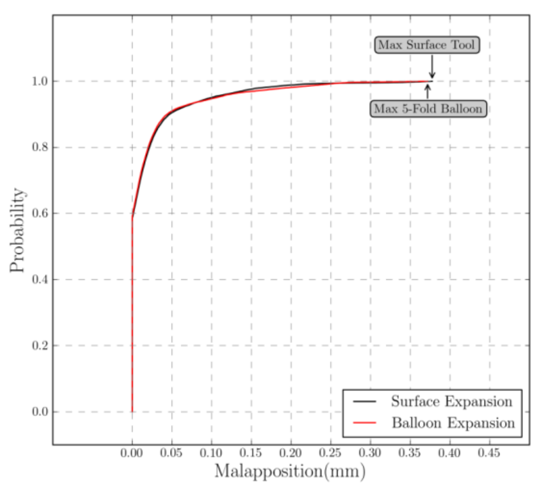

Figure 13. Cumulative distribution functions (CDF) were plotted after each expansion step measuring

the stent malapposition. The CDF graphs are almost identical demonstrating that for this patient specific case, a deformable surface could be used for simplicity.